

Article

Solvation Dynamics of CO₂(g) by Monoethanolamine at the Gas–Liquid Interface: A Molecular Mechanics Approach

I-Shou Huang, Jia-Jen Li and Ming-Kang Tsai *

Department of Chemistry, National Taiwan Normal University, Taipei 11677, Taiwan;
FerrisWhiston@gmail.com (I-S.H.); sophy0956@gmail.com (J.-J.L.)

* Correspondence: mktsai@ntnu.edu.tw; Tel.: +886-2-77346217

Academic Editor: Steve Scheiner

Received: 26 October 2016; Accepted: 19 December 2016; Published: 23 December 2016

Abstract: A classical force field approach was used to characterize the solvation dynamics of high-density CO₂(g) by monoethanolamine (MEA) at the air–liquid interface. Intra- and intermolecular CO₂ and MEA potentials were parameterized according to the energetics calculated at the MP2 and BLYP-D2 levels of theory. The thermodynamic properties of CO₂ and MEA, such as heat capacity and melting point, were consistently predicted using this classical potential. An approximate interfacial simulation for CO₂(g)/MEA(l) was performed to monitor the depletion of the CO₂(g) phase, which was influenced by amino and hydroxyl groups of MEA. There are more intramolecular hydrogen bond interactions notably identified in the interfacial simulation than the case of bulk MEA(l) simulation. The hydroxyl group of MEA was found to more actively approach CO₂ and overpower the amino group to interact with CO₂ at the air–liquid interface. With artificially reducing the dipole moment of the hydroxyl group, CO₂–amino group interaction was enhanced and suppressed CO₂(g) depletion. The hydroxyl group of MEA was concluded to play dual but contradictory roles for CO₂ capture.

Keywords: CO₂ capture; alcoholamine; molecular mechanics; interface; dynamics

1. Introduction

Monoethanolamine (MEA) is extensively used in the electric power industry for directly scrubbing CO₂ from the exhaust gas produced by fossil fuel combustion [1]. MEA nucleophilically attacks the partially positively charged carbon atom of CO₂ with its amino groups, forming the zwitterionic (ZW) intermediate of [HOCH₂CH₂NH₃⁺CO₂[−]], thereby pulling CO₂ from the exhaust gas. This ZW intermediate subsequently stabilizes itself by transferring a proton from its quaternary nitrogen through an intermolecular hydrogen bond (HB) network to other proton acceptors. Such a network can be formed by a combination of the amino or hydroxyl groups of MEA or with other additives that can form HBs. Water and other types of alcoholamines, such as diethanolamines (DEAs) and methyl-diethanolamines (MDEAs), are common additives in MEA solutions to improve overall CO₂ scrubbing efficiency.

MEA is widely produced by controlling the stoichiometry of ethylene oxide reacting with aqueous ammonia. Secondary or tertiary amines can be generated by increasing the ethylene oxide:ammonia ratio. Several studies have performed experimental characterizations [2–14] and computational investigations [15–17] to elucidate and improve CO₂-scrubbing reactivity by using various types of alcoholamines. The engineering of various functionalized ethylene oxides as the starting materials at the industrial scale to synthesize the designed alcoholamines can be challenging. Conway et al. measured the kinetic rate and equilibrium constants of CO₂ (aq) with various sterically hindered alcoholamines and determined iso-butylamine, *n*-butylamine, and *n*-propylamine to be the

main scrubbers for the CO₂ binding step; none of the three amines contain hydroxyl groups [13]. A hydroxylated compound, 3-amino-1-propanol (MPA), was observed to be approximately 20% less efficient at binding CO₂ (aq) compared with the aforementioned amines. Intuitively, elongating the alcohol groups, such as MPA in respect to and MEA, can improve CO₂ binding affinity. Li and Tsai performed molecular dynamics simulations and stated that an appropriate length of the alkyl chain between the amino and hydroxyl groups can minimize the electronic cancellation effect from the two electron-withdrawing groups [18]. Adding water molecules to alcoholamines can facilitate the deprotonation process [19] and stabilize the ZW intermediates. However, water molecules can also potentially compete for the CO₂ absorption sites by forming intermolecular HBs with the amino groups [18]. If the basicity of alcoholamines is adequately strong, water can be deprotonated to form OH⁻ and protonated alcoholamines, where OH⁻ is known to bind CO₂ efficiently.

Considering the aforementioned observations, the hydroxyl groups of alcoholamines seem to play a trivial role for CO₂ capture. However, because of the use of ethylene oxide as the starting material for synthesizing alcoholamines, the hydroxyl groups are inherently present in CO₂ scrubbers. Compared with the CO₂-binding characteristic of the amino groups, the hydroxyl groups can shuttle protons from the quaternary nitrogen of the ZW intermediates to the CO₂⁻ moieties, as shown by *ab initio* molecular dynamic simulations of CO₂ in neat MEA liquid [20]. However, this proton transfer capability of the hydroxyl groups is anticipated to be less effective compared with that of water molecules.

Several studies have performed computational modeling of the CO₂ capture phenomena at the nanometer and nanosecond scales by using a classical force field approach [21]. Most of these studies primarily focused on predicting the CO₂ transport property and fixation phenomena through physical absorption in various solutions, such as CO₂, H₂O, and a mixture of different types of alcoholamine derivatives. Jhon et al. predicted the nucleophilicities and accessibilities of MEA, 2-methylaminoethanol, and 2-amino-2-methyl-1-propanol, and emphasized that the predicted CO₂-binding reactivity correlates with the accuracy of describing the steric effect of amines by the chosen force field [22]. Turgman-Cohen et al. included the ionic species that resulted from CO₂ chemisorption in the model and qualitatively mimicked the thermogravimetric experiments [23]. Farmahini et al. simulated the separation of CO₂ and CH₄ mixtures in MDEA solution, which was accelerated piperazine [24]. Yu et al. developed a synergistic molecular dynamics model and reported that an optimal ternary mixture outperformed other quaternary or quintuple amine systems in the realm of CO₂ diffusivity [25].

Extensive computational studies have focused on improving CO₂-binding efficiency by using amino groups; however, the roles of the hydroxyl groups of alcoholamines have not been fully characterized. Notably, Du et al. measured the surface vibrational spectrum by using the sum frequency generation technique to address the hydrophobicity of the air–water interface and identified the spectroscopic fingerprint of the dangling hydroxyl groups [26]. Electrostatic interactions resulting from such dangling hydroxyl groups at the air–water interface favored the solvation of anionic ions, as previously reported [27–33]. Thus, the solvation phenomena of nonpolar CO₂ molecules containing the quadruple moment at the air–alcoholamine interface inspired the present study. Pure CO₂(g) can be considered a hydrophobic phase, whereas scrubber alcoholamines are highly hydrophilic because of the presence of amino and hydroxyl groups. Understanding the dynamic details of removing CO₂ molecules from the hydrophobic environment to be subsequently solvated and absorbed by hydrophilic alcoholamines can provide the underlying microscopic characteristics of these organic scrubbers.

Therefore, we conducted all-atom molecular dynamic simulations to model CO₂ solvation dynamics at the air–liquid interface. We started from the MM3 force field [34–39], a classical molecular mechanics force field for hydrocarbons, and modified the required parameters for CO₂ and MEA molecules, then benchmarked the CO₂ potential in the gas phase, MEA(l) potential in the solution phase, and the CO₂–MEA absorption pathway compared with density functional theory (DFT) results. Finally, we monitored the dynamics of the CO₂(g)/MEA(l) interface. Proton transfer from the ZW intermediates for the subsequent chemical absorption step was omitted in this study due to the

complexity of parameterizing the reactive force fields. The present study has focused at the dominant physical absorption phenomena of CO₂ molecules at the air–liquid interface.

2. Results and Discussion

2.1. Benchmark Using CO₂ and (CO₂)₂ Models

The intermolecular interactions between CO₂ molecules of three selected characteristic structures—namely, the global minimum, parallel, and T-type (CO₂)₂ structures in Figure 1—were compared at the BLYP-D2, MP2, and molecular mechanics (MM) levels of theory in Table 1. Geometric constraints were imposed for optimizing the parallel and T-type structures. The intermolecular interactions (E_{int}) characterized at the MM level were compared using the binding energies (BE) of the BLYP-D2 or MP2 levels. For the global minimum structure of (CO₂)₂, E_{int} was predicted to be −1.23 kcal/mol versus −1.06 and −1.27 kcal/mol at the BLYP-D2 and MP2 levels, respectively. The parallel (CO₂)₂ structure with C–C constrained at 4.0 Å was the most repulsive one, where the MM level (0.16 kcal/mol) qualitatively reproduced the interaction, as predicted at the BLYP-D2 and MP2 levels (0.25 and −0.01 kcal/mol). T-type (CO₂)₂ was consistently predicted to interact less strongly than the global minimum at all three levels. The current nonpolarizable MM approach dominantly contributed through dipole–dipole (μμ) interactions for intermolecular CO₂ interactions, but van der Waals (vdW) interactions primarily contributed to the BE of BLYP-D2 and MP2 levels. Using the functional forms of classical electrostatic and Lennard–Jones (LJ) potentials to distinguish the electrostatic and vdW contributions have been reported as challenging in the case of water model development [40–43]. The success of such distinction is mainly subject to the selected functional form for the classical representation of vdW interactions. Thus, further improvement of current CO₂ potential is in progress and not included in the scope of this study. Nonetheless, the total intermolecular CO₂ interaction calculated by MM still remained a reasonable agreement with the quantum mechanical (QM) results. Finally, vibrational frequencies of the CO₂ monomer calculated at the MM level were consistent with those calculated at the BLYP-D2 and MP2 levels.

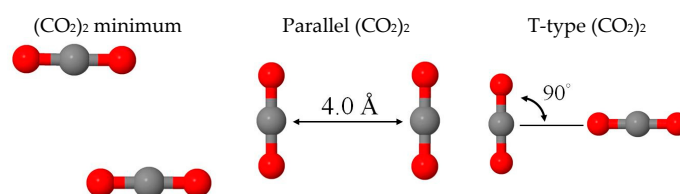


Figure 1. Schematic representation of the minimum, parallel and T-type (CO₂)₂ structures.

Table 1. Comparison of CO₂ monomeric and dimeric models at the BLYP-D2, MP2, and molecular mechanics (MM) levels (kcal/mol).

¹ Isomers	Min	Parallel	T-Type	ν_{CO_2} (cm ^{−1})
² BE(BLYP-D2)	−1.06	0.25	−0.77	636, 1302, 2310
BE(BLYP)	0.29	0.76	0.09	
BE(displacement)	−1.36	−0.50	−0.86	
² BE(MP2)	−1.27	−0.01	−1.07	668, 1310, 2374
BE(HF)	−0.05	0.83	−0.16	
BE(displacement)	−1.22	−0.84	−0.91	
³ E _{int} (MM)	−1.23	0.16	−0.92	629, 1240, 2374
E _{int} ^{MM} _{μμ}	−1.00	0.32	−0.70	
E _{int} ^{MM} _{LJ}	−0.23	−0.15	−0.22	

¹ Graphical representation of the (CO₂)₂ models is presented in Figure 1. ² Binding energy (BE) (BLYP-D2 and MP2) contains the correction of the basis set superposition error by using BLYP-D2 and MP2 optimized structures, respectively. ³ E_{int} denotes the interaction energy at the MM level, where μμ and LJ denote dipole–dipole and Lennard–Jones terms, respectively.

2.2. Phase Transition of (CO₂)₁₃

The phase transition temperature of (CO₂)₁₃ clusters was characterized to benchmark the thermodynamic property prediction by using the current CO₂ potential. Maillet et al. reported the melting transition of (CO₂)₁₃ at 95 K [44]. Liu and Jordan observed the solid–solid phase transition at approximately 90 K [45] by using a two-body model developed by Murthy et al. [46]. Murthy potential is a two-body potential using a rigid monomer, 5-point electrostatic sites, and atomic 6–12 Lennard–Jones terms. Comparably, the current CO₂ model showed vibrational capability, with atomic 6–12 Lennard–Jones terms and bond-centered dipole–dipole ($\mu\mu$) interactions. The calculated heat capacity curve from 88 K to 97 K of (CO₂)₁₃ clusters is shown in Figure 2. Each canonical ensemble (NVT) simulation was pre-equilibrated for 2.5 ns and sampled for 100 ns at a 0.5-fs time step. A solid–solid phase transition was identified at 91 K, followed by cluster evaporation beyond 97 K. The heat capacity was calculated using Equation 1.

$$C_{\text{NVT}}(T) = \frac{\langle U^2 \rangle - \langle U \rangle^2}{N_A k_B T^2} \quad (1)$$

where U is the sampled potential energy of (CO₂)₁₃, N_A is the Avogadro constant, k_B is the Boltzmann constant, $\langle U^2 \rangle$ and $\langle U \rangle^2$ denote the mean of U^2 and the square of the average U , respectively.

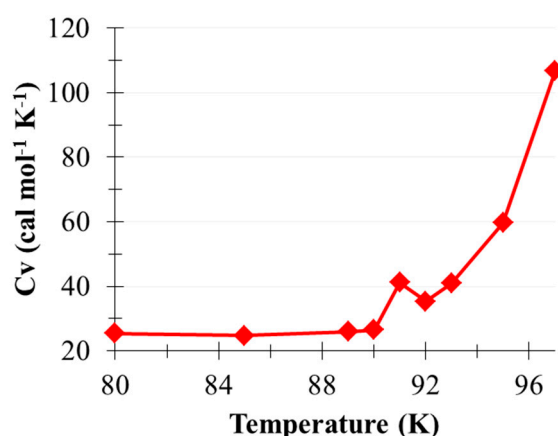


Figure 2. Heat capacity curve of (CO₂)₁₃ clusters predicted using molecular dynamic simulations.

2.3. Benchmark of the MEA Potential

Three stable geometries are identified for the monomeric MEA at MP2/aug-cc-pVTZ with the polarizable continuum model (PCM) as shown in Figure S1. One of the *cis*-form MEA monomers containing an intramolecular hydrogen bond (intraHB) interaction between OH \cdots NH₂ is predicted to be the lowest energy at MP2 level. The energetics between these three stable geometries are calculated to be deviated by a trivial difference at both MP2 and MM levels, as summarized at Table S1 in Supplementary Materials. Two hydrogen-bonded geometries, denoted as NHN and OHO, were selected for comparing the current MEA potential at the MM level with BLYP-D2, as shown in Figure 3. Constrained optimizations were conducted to converge the minimum geometry searching with the XH \cdots X angle frozen at 180°. The intermolecular interactions between two MEA molecules are summarized in Table 2. The binding energy of OHO was predicted to be stronger than that of NHN at -6.90 and -6.15 kcal/mol for the BLYP-D2 and MM levels, respectively. NHN interactions were estimated to be -4.62 and -4.16 kcal/mol for the BLYP-D2 and MM levels, respectively. Even by using the BLYP-D2-optimized geometry, the MM level predicted acceptable interactions compared with the MM-optimized geometry, as shown by ¹Eint versus ²Eint in Table 2. This consistency indicated strong similarity between the two constrained optimized geometries at the BLYP-D2 and MM levels. However,

weak contribution to the intermolecular binding from the vdW interactions was still in presence for the current MEA potential. Phase transition of the (MEA)₁₂₈ model was simulated to investigate the thermodynamic property prediction by using the current MEA model. Eight NVT simulations were performed at 280–420 K, with a density of 1.01 g/cm³. Each run was pre-equilibrated and sampled for 3 ns to predict the corresponding heat capacity. A phase transition was identified at approximately 320 K as shown in Figure 4, and the experimental freezing point of MEA(l) was 283 K [47]. Thus, the current MEA potential slightly overestimated the melting property of MEA.

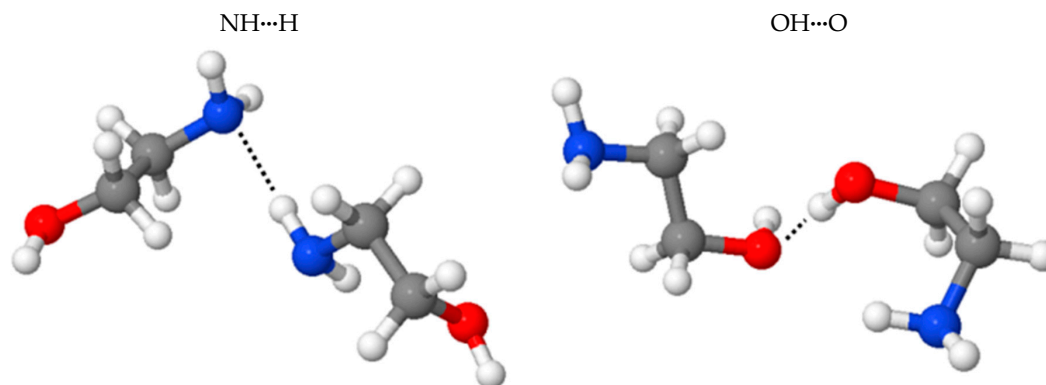


Figure 3. Constrained optimized geometries of (MEA)₂ at the BLYP-D2/aug-cc-pVTZ level. MEA: monoethanolamine.

Table 2. Comparison of intermolecular interactions between the BLYP-D2 and MM levels (kcal/mol).

Isomers ³	NHN	OHO
¹ BE(BLYP-D2)	−4.62	−6.90
¹ BE(BLYP)	−1.35	−3.50
¹ BE(disp)	−3.28	−3.32
¹ Eint _{MM} ^{MM}	−1.85	−3.61
¹ Eint _{VDM} ^{MM}	−1.88	−1.40
² Eint _{Total} ^{MM}	−4.16	−6.15
² Eint _{MM} ^{MM}	−2.17	−4.33
² Eint _{VDM} ^{MM}	−1.99	−1.82

¹ Constrained optimized geometry at the BLYP-D2/aug-cc-pVTZ level. ² Constrained optimized geometry at the MM level. ³ The same notation is adopted as that in Table 1.

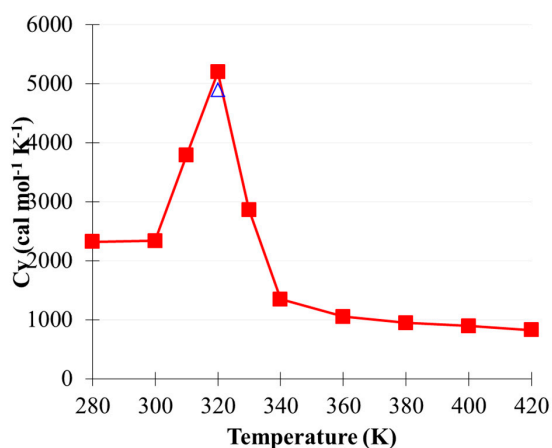


Figure 4. Heat capacity curve of the (MEA)₁₂₈ model predicted using molecular dynamic simulation. The triangle denotes another independent 320 K simulation.

2.4. CO₂ Binding Using MEA

Constrained optimizations in the gas phase along the C_{CO₂}-N_{MEA} distance were calculated at both the BLYP-D2 and MM levels along the CO₂-binding pathway. The relative energetics considering each physical absorption minimum structure at both levels is summarized in Figure 5. CO₂ was physically absorbed at a distance of approximately 2.9 Å from N_{MEA} at the BLYP-D2/aug-cc-pVTZ level and approximately 2.7 Å for the case predicted at the MM level. Close agreement was observed between the two theory levels for the C_{CO₂}-N_{MEA} distance (r_{CN}) ranging from 2.8 to 2.2 Å. At $r_{CN} = 2.0$ Å, MM showed more than 2.5 kcal/mol deviated from BLYP-D2. This deviation exponentially increased as r_{CN} increased beyond 2.0 Å. Natural population analysis was performed to estimate the fragment charge of the amino group of MEA (q_{NH_2}) and CO₂ (q_{CO_2}) along the absorption pathway, as plotted at the secondary y -axis in Figure 5. At $r_{CN} = 2.2$ –2.8 Å, q_{NH_2} and q_{CO_2} slightly varied. However, considerable increases and decreases were observed for q_{NH_2} and q_{CO_2} beyond $r_{CN} = 2.0$ Å, respectively, suggesting a substantial charge transfer effect as CO₂ approached the amino group of MEA. The current nonpolarizable potential did not consider such electronic redistribution, regardless of the reparameterization of the balance between electrostatic and vdW interactions in this approach. Thus, marked deviations were anticipated between the MM and BLYP-D2 levels. Nonetheless, the accuracy of the current potential was reasonable at $r_{CN} > 2.0$ Å.

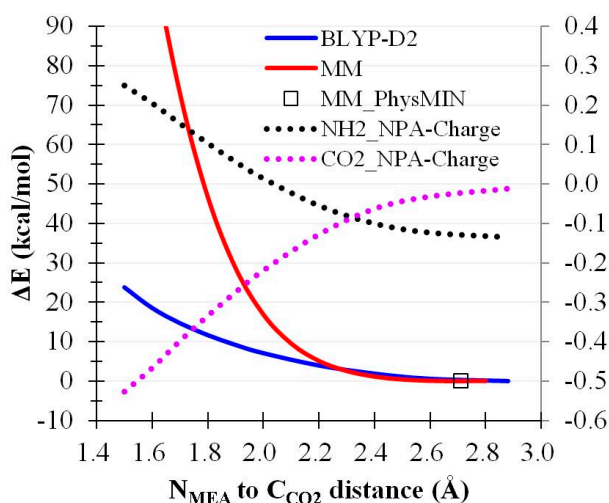


Figure 5. Relative energetics of CO₂ binding by MEA in the gas phase (kcal/mol).

2.5. CO₂(g) Dissolution by MEA(l)

A conceptual interfacial model using high-density CO₂(g) surrounded by MEA(l) was characterized to study the solvation dynamics of CO₂ in MEA(l). CO₂(g) represented by a (CO₂)₄₄ cluster model was equilibrated at 400 K for 4 ns under NVT ensemble. A repulsive spherical potential ($r = 9.1257$ Å) was applied, and the sphere density was fixed at 1.01 g/cm³. The final atomic coordinates and velocities of the (CO₂)₄₄ cluster were adopted for the subsequent CO₂(g)/MEA(l) simulation. A 4 ns NVT simulation of (MEA)₈₆₄ under the periodic boundary condition, $T = 400$ K, and density = 1.01 g/cm³ was conducted for creating the MEA(l) model. The MEA molecules located within $r = 9.5$ Å were removed from the final structure of (MEA)₈₆₄ simulation, and an (MEA)₈₀₄ model was obtained by adopting the corresponding atomic velocities. Finally, the initial condition of the CO₂(g)/MEA(l) simulation was generated by combining the (CO₂)₄₄ cluster and (MEA)₈₀₄ model by using the same cell size as that of the (MEA)₈₆₄ simulation, as shown in Figure 6.

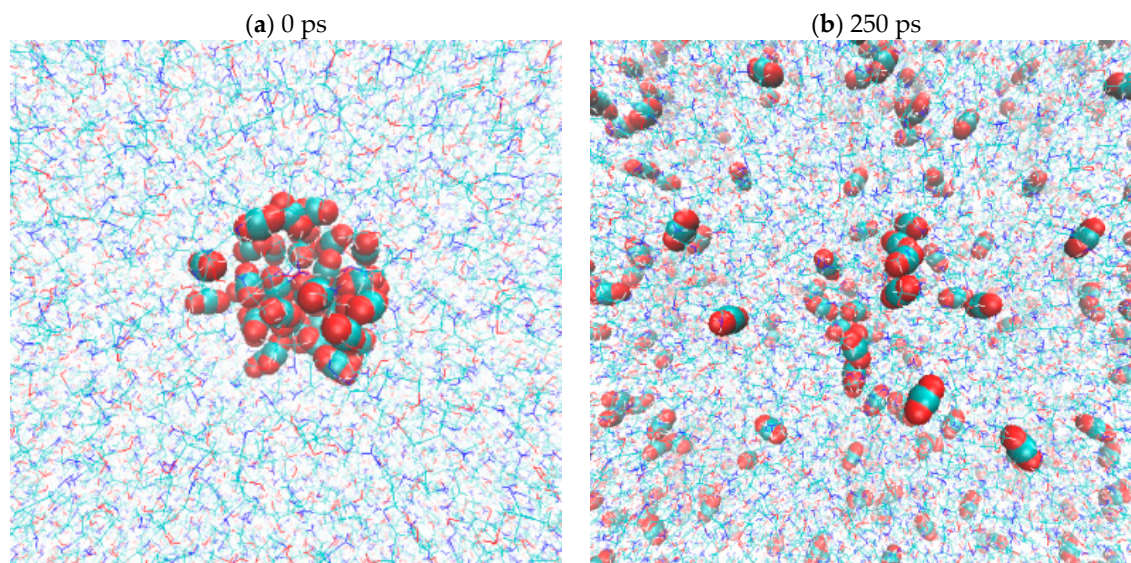


Figure 6. Schematic representation of the initial and final snapshots of $\text{CO}_2(\text{g})$ dissolved in $\text{MEA}(\text{l})$.

A 250 ps simulation using the isoenthalpic-isobaric ensemble (NPH) was subsequently conducted for the interfacial $\text{CO}_2(\text{g})/\text{MEA}(\text{l})$ model. The external pressure of the NPH ensemble was 7415 atm, according to the average value of the previous $(\text{MEA})_{864}$ NVT simulation. Radial distribution functions, $g(r)$, of $\text{C}_{\text{CO}_2}\text{-C}_{\text{CO}_2}$, $\text{C}_{\text{CO}_2}\text{-N}_{\text{NH}_2}$, and $\text{C}_{\text{CO}_2}\text{-O}_{\text{OH}}$, denoted as $g_{\text{C}_{\text{CO}_2}\text{C}_{\text{CO}_2}}^{\text{orig}}(r)$, $g_{\text{C}_{\text{CO}_2}\text{N}_{\text{NH}_2}}^{\text{orig}}(r)$, and $g_{\text{C}_{\text{CO}_2}\text{O}_{\text{OH}}}^{\text{orig}}(r)$, were plotted considering the simulation time, as shown in Figure 7. Multiple $g(r)$ results were analyzed for various time periods (0, 20, 40, 60, 80, 100, 120, 150, 200, and 250 ps), as shown in the legends. In Figure 7a, $g_{\text{C}_{\text{CO}_2}\text{C}_{\text{CO}_2}}(r)$ substantially increased for the $r_{\text{C}_{\text{CO}_2}\text{C}_{\text{CO}_2}} > 16 \text{ \AA}$ region after 250 ps simulation, and this increase represented the depletion kinetics of high-density $\text{CO}_2(\text{g})$. The profound $g_{\text{C}_{\text{CO}_2}\text{C}_{\text{CO}_2}}^{\text{orig}}(r = 3.7 \text{ \AA})$ indicated the presence of a CO_2 clustering effect. Such an effect is considered to diminish with the increasing simulation time because of the stronger interaction of $\text{CO}_2\text{-MEA}$ than of $\text{CO}_2\text{-CO}_2$. Between $g_{\text{C}_{\text{CO}_2}\text{N}_{\text{NH}_2}}^{\text{orig}}(r)$ and $g_{\text{C}_{\text{CO}_2}\text{O}_{\text{OH}}}^{\text{orig}}(r)$, the probability of CO_2 binding was higher by the hydroxyl group than by amino groups of MEA. Notably, such a difference cannot be attributed to the binding energy of CO_2 to the amino and hydroxyl groups of MEA because the intermolecular interaction of CO_2 with the binding motif at the MM level was 5.50 and 5.05 kcal/mol, respectively. According to 250 ps simulation, the hydroxyl groups contributed more to the depletion of the $(\text{CO}_2)_{44}$ cluster and suppression of the interactions between the CO_2 and amino groups.

A control experiment using 250 ps $\text{CO}_2(\text{g})/\text{MEA}(\text{l})$ simulation was performed to clarify the role of the hydroxyl groups of MEA, in which μ_{OH} was scaled down by 90% and other parameters were the same as those in prior unscaled simulation. The resulting $g(r)$ of $\text{C}_{\text{CO}_2}\text{-C}_{\text{CO}_2}$, $\text{C}_{\text{CO}_2}\text{-N}_{\text{NH}_2}$, and $\text{C}_{\text{CO}_2}\text{-N}_{\text{OH}}$, denoted as $g_{\text{C}_{\text{CO}_2}\text{C}_{\text{CO}_2}}^{\text{sc}}(r)$, $g_{\text{C}_{\text{CO}_2}\text{N}_{\text{NH}_2}}^{\text{sc}}(r)$, and $g_{\text{C}_{\text{CO}_2}\text{N}_{\text{OH}}}^{\text{sc}}(r)$, are summarized in Figure 7d–f. Figure 7d shows that the $g_{\text{C}_{\text{CO}_2}\text{C}_{\text{CO}_2}}^{\text{sc}}(3.7)$ peak was substantially higher than $g_{\text{C}_{\text{CO}_2}\text{C}_{\text{CO}_2}}^{\text{orig}}(3.7)$ at the end of 250 ps, suggesting the presence of a stronger CO_2 clustering effect. In other words, $\text{CO}_2(\text{g})$ depletion was suppressed because of weak $\mu_{\text{OH}} \bullet \bullet \mu_{\text{C}=\text{O}}$ interactions. The physical absorption of CO_2 by the amino groups was markedly enhanced, as observed in $g_{\text{C}_{\text{CO}_2}\text{N}_{\text{NH}_2}}^{\text{sc}}(2.8)$ in Figure 7e. The probability of CO_2 being physically absorbed by the hydroxyl groups was observed at further $r_{\text{C}_{\text{CO}_2}\text{O}}$ distance by $g_{\text{C}_{\text{CO}_2}\text{N}_{\text{OH}}}^{\text{sc}}(3.0)$ compared with $g_{\text{C}_{\text{CO}_2}\text{O}_{\text{OH}}}^{\text{orig}}(2.7)$ in Figure 7c of the unscaled case. The time evolution of $g_{\text{C}_{\text{CO}_2}\text{C}_{\text{CO}_2}}^{\text{orig}}(3.65)$ and $g_{\text{C}_{\text{CO}_2}\text{C}_{\text{CO}_2}}^{\text{sc}}(3.65)$ was compared with consideration of the simulation time, as shown in Figure 8, and $\text{CO}_2(\text{g})$ depletion was substantially enhanced because of the introduction of the reduced μ_{OH} of MEA molecules.

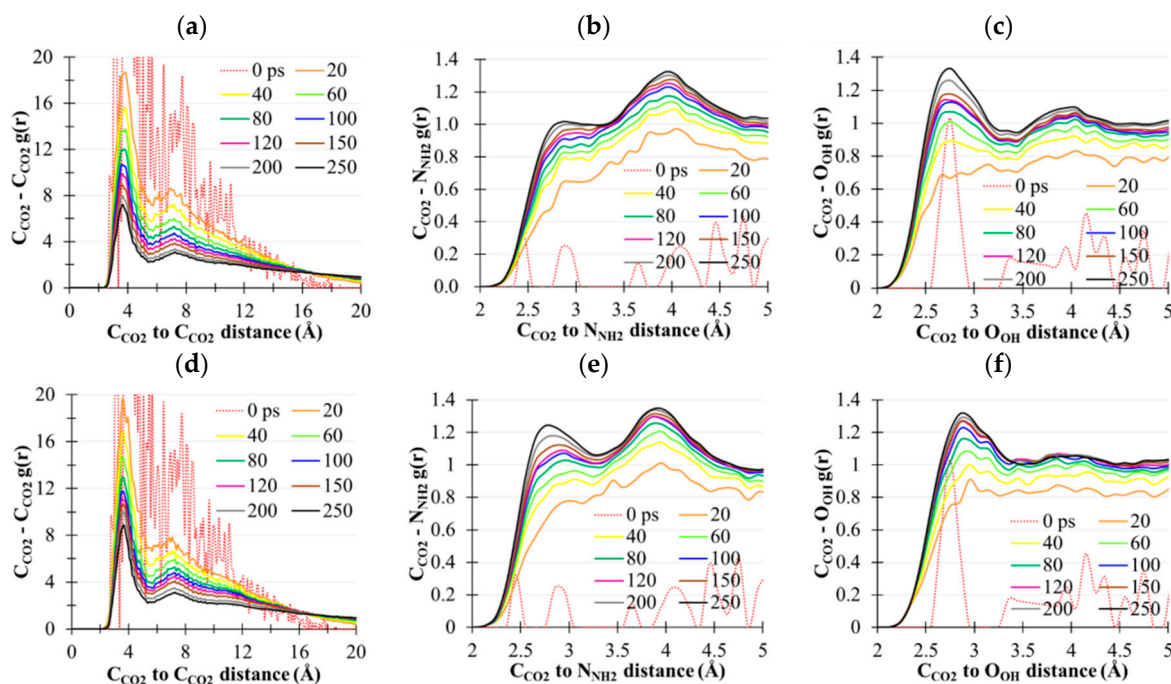


Figure 7. Radial distribution functions of $C_{CO_2}-C_{CO_2}$, $C_{CO_2}-N_{NH_2}$, and $C_{CO_2}-O_{OH}$ calculated at various time periods. (a–c) shows the unscaled μ_{OH} and (d–f) shows 10% μ_{OH} .

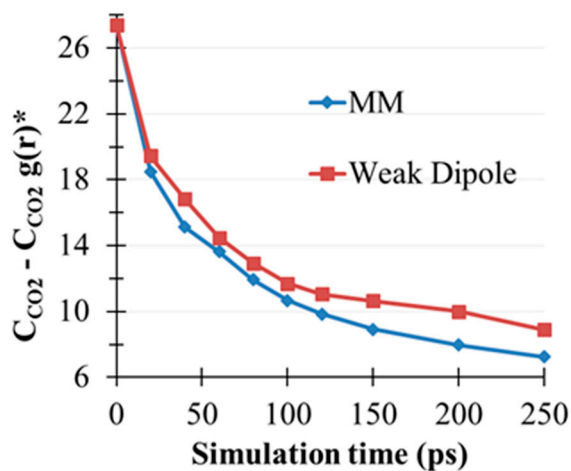


Figure 8. Time evolution for $g(r)$ of $C_{CO_2}-C_{CO_2}$ at $r_{C_{CO_2}C_{CO_2}} = 3.65 \text{ \AA}$ for the original and scaled simulations.

The geometries of MEA molecules containing the intramolecular hydrogen bond interactions are analyzed for the 2 ns bulk MEA simulation and the first 200 ps of the $CO_2(g)/MEA(l)$ simulation. Two hundred snapshots are recorded for each case where 10 MEA molecules are selected and monitored out of these recorded snapshots. The histograms of the intramolecular $N_{NH_2}-H_{OH}$ distance ($r_{intraNH}$) are recorded in Figure S2 (10×200 data points are included at each figure). By comparing the recorded data points of $r_{intraNH} < 2.2 \text{ \AA}$, the $CO_2(g)/MEA(l)$ simulation contains substantially more intraHB geometries during the first 200 ps over the case of bulk MEA simulation. The less hydrophilic CO_2 phase could stabilize the presence of intraHB MEA orientations, while the bulk MEA liquid could favor the intermolecular hydrogen bond interactions.

3. Experimental Section

Molecular mechanics (MM) calculations were performed using Tinker version 7.1 [48]. Force field parameters for MEA and CO₂ adopted the relevant fragments defined in MM3 force field, followed by comprehensive reparameterization routines in order to maximize the agreement with the quantum mechanical (QM) calculations at MP2 or DFT levels for the hydrogen-bonded complexes of (MEA)₂ and the CO₂••MEA physically absorbed structure, as discussed below. MM3 was originally designed for describing hydrocarbons and thus provided a good starting point for the subsequent parameterizations [34–39]. BLYP functional [49,50] augmented with Grimme's D2 dispersion correction [51], being reported to appropriately describe CO₂–alcoholamine interactions by using a triple-zeta quality basis set, was adopted for the DFT calculations [52]. The CO₂ parameters took into account molecular stretching and bending motions, interatomic Lennard–Jones interactions, and bond-centered dipole–dipole interactions. The interatomic van der Waals (vdW) interactions were described using the arithmetic and geometric combining rules for radius and epsilon, respectively. The cutoff values of vdW and dipole–dipole interactions were set at 10.0 and 12.0 Å, respectively. Berendsen thermostat was used for the molecular dynamic simulations with a coupling time of 0.1 ps [53]. All electronic structure calculations in this study were performed using the GAUSSIAN 09 package [54]. MP2 and BLYP-D2 calculations used the aug-cc-pVTZ basis set.

4. Conclusions

In the present study, a nonpolarizable MM approach was reported to characterize CO₂(g) dissolution in MEA(l). The current CO₂ and MEA potentials showed reasonable agreement with the MP2 and BLYP-D2 levels of theory for describing the intramolecular vibration and intermolecular interactions of CO₂, (CO₂)₂, and (MEA)₂. Heat capacity simulations by using (CO₂)₁₃ clusters reproduced the solid–solid phase transition at approximately 90 K, as reported in previous studies. The melting transition predicted using the (MEA)₁₂₈ model was approximately 320 K, in which the experimental freezing potential of pure MEA was 283 K. Along the CO₂ absorption pathway by MEA, the MM approach reproduced the energetics of the BLYP-D2 level if CO₂ was bound at a distance of approximately 2.0 Å from the amino group of MEA. The absence of polarizable terms in the current potential could not describe the charge transfer effect, which was included in the BLYP-D2 level of theory, because CO₂ was absorbed by MEA at a short C_{CO2} to N_{MEA} distance (<2.0 Å).

At the gas–liquid interface represented by the (CO₂)₄₄ and (MEA)₈₀₄ models, CO₂(g) was almost completely depleted within 250 ps. There are notably more intramolecular hydrogen bond interactions identified than the case of bulk MEA simulation. The hydroxyl groups of MEA more actively approached CO₂ at the interfacial region and suppressed the absorption probability of the NH groups. The artificial reduction of the dipole moment of the hydroxyl bonds enhanced CO₂–amino group interactions, but the depletion of CO₂ gas phase was reduced as well. The hydroxyl groups of MEA were identified to play contradictory roles in the interfacial CO₂ capture process. The current findings could provide additional perspectives for the synthetic design of molecular CO₂ scrubbers.

Supplementary Materials: The following are available online at: <http://www.mdpi.com/1420-3049/22/1/8/s1>. optimized geometries of MEA monomer at MP2 and MM levels; histograms of potential interHB geometries in the MD simulations; Cartesian coordinates at BLYP-D2/aug-cc-pVTZ level for the OHO and NHN; force field parameters for CO₂ + MEA

Acknowledgments: This study was supported by the Ministry of Science and Technology of Taiwan (103-2113-M-003-005-MY2 and 105-2113-M-003-010). MKT is grateful to the National Center for High-Performance Computing of Taiwan for providing computer time and facilities.

Author Contributions: I-S.H. and J.-J.L. conducted the simulations and analyzed the data; M.-K.T. designed the simulations and analysis procedure, and wrote the paper.

Conflicts of Interest: The authors declare no conflict of interest.

References

1. Rochelle, G.T. Amine scrubbing for CO₂ capture. *Science* **2009**, *325*, 1652–1654. [[CrossRef](#)] [[PubMed](#)]
2. Yih, S.M.; Shen, K.P. Kinetics of carbon-dioxide reaction with sterically hindered 2-amino-2-methyl-1-propanol aqueous-solutions. *Ind. Eng. Chem. Res.* **1988**, *27*, 2237–2241. [[CrossRef](#)]
3. Alper, E. Reaction-mechanism and kinetics of aqueous-solutions of 2-amino-2-methyl-1-propanol and carbon-dioxide. *Ind. Eng. Chem. Res.* **1990**, *29*, 1725–1728. [[CrossRef](#)]
4. Tontiwachwuthikul, P.; Meisen, A.; Lim, C.J. CO₂ absorption by naoh, monoethanolamine and 2-amino-2-methyl-1-propanol solutions in a packed column. *Chem. Eng. Sci.* **1992**, *47*, 381–390. [[CrossRef](#)]
5. Saha, A.K.; Bandyopadhyay, S.S.; Biswas, A.K. Kinetics of aasorption of CO₂ into aqueous-solutions of 2-amino-2-methyl-1-propanol. *Chem. Eng. Sci.* **1995**, *50*, 3587–3598. [[CrossRef](#)]
6. Messaoudi, B.; Sada, E. Kinetics of absorption of carbon dioxide into aqueous solutions of sterically hindered 2-amino-2-methyl-1-propanol. *J. Chem. Eng. Jpn.* **1996**, *29*, 193–196. [[CrossRef](#)]
7. Xu, S.; Wang, Y.W.; Otto, F.D.; Mather, A.E. Kinetics of the reaction of carbon dioxide with 2-amino-2-methyl-1-propanol solutions. *Chem. Eng. Sci.* **1996**, *51*, 841–850. [[CrossRef](#)]
8. Seo, D.J.; Hong, W.H. Effect of piperazine on the kinetics of carbon dioxide with aqueous solutions of 2-amino-2-methyl-1-propanol. *Ind. Eng. Chem. Res.* **2000**, *39*, 2062–2067. [[CrossRef](#)]
9. Xiao, J.; Li, C.W.; Li, M.H. Kinetics of absorption of carbon dioxide into aqueous solutions of 2-amino-2-methyl-1-propanol plus monoethanolamine. *Chem. Eng. Sci.* **2000**, *55*, 161–175. [[CrossRef](#)]
10. Mandal, B.P.; Bandyopadhyay, S.S. Simultaneous absorption of carbon dioxide and hydrogen sulfide into aqueous blends of 2-amino-2-methyl-1-propanol and diethanolamine. *Chem. Eng. Sci.* **2005**, *60*, 6438–6451. [[CrossRef](#)]
11. Mandal, B.P.; Bandyopadhyay, S.S. Absorption of carbon dioxide into aqueous blends of 2-amino-2-methyl-1-propanol and monoethanolamine. *Chem. Eng. Sci.* **2006**, *61*, 5440–5447. [[CrossRef](#)]
12. Barzagli, F.; Mani, F.; Peruzzini, M. A ¹³C nmr study of the carbon dioxide absorption and desorption equilibria by aqueous 2-aminoethanol and n-methyl-substituted 2-aminoethanol. *Energy Environ. Sci.* **2009**, *2*, 322–330. [[CrossRef](#)]
13. Conway, W.; Wang, X.; Fernandes, D.; Burns, R.; Lawrance, G.; Puxty, G.; Maeder, M. Toward the understanding of chemical absorption processes for post-combustion capture of carbon dioxide: Electronic and steric considerations from the kinetics of reactions of CO₂(aq) with sterically hindered amines. *Environ. Sci. Technol.* **2013**, *47*, 1163–1169. [[CrossRef](#)] [[PubMed](#)]
14. Choi, Y.-S.; Im, J.; Jeong, J.K.; Hong, S.Y.; Jang, H.G.; Cheong, M.; Lee, J.S.; Kim, H.S. CO₂ absorption and desorption in an aqueous solution of heavily hindered alkanolamine: Structural elucidation of CO₂-containing species. *Environ. Sci. Technol.* **2014**, *48*, 4163–4170. [[CrossRef](#)] [[PubMed](#)]
15. Mindrup, E.M.; Schneider, W.F. Computational comparison of the reactions of substituted amines with CO₂. *ChemSusChem* **2010**, *3*, 931–938. [[CrossRef](#)] [[PubMed](#)]
16. Lee, A.S.; Kitchin, J.R. Chemical and molecular descriptors for the reactivity of amines with CO₂. *Ind. Eng. Chem. Res.* **2012**, *51*, 13609–13618. [[CrossRef](#)]
17. Gangarapu, S.; Marcelis, A.T.M.; Zuilhof, H. Carbamate stabilities of sterically hindered amines from quantum chemical methods: Relevance for CO₂ capture. *Chemphyschem* **2013**, *14*, 3936–3943. [[CrossRef](#)] [[PubMed](#)]
18. Li, H.-C.; Tsai, M.-K. A first-principle study of CO₂ binding by monoethanolamine and mono-n-propanolamine solutions. *Chem. Phys.* **2015**, *452*, 9–16. [[CrossRef](#)]
19. Guido, C.A.; Pietrucci, F.; Gallet, G.A.; Andreoni, W. The fate of a zwitterion in water from ab initio molecular dynamics: Monoethanolamine (mea)-CO₂. *J. Chem. Theory Comput.* **2013**, *9*, 28–32. [[CrossRef](#)] [[PubMed](#)]
20. Han, B.; Sun, Y.; Fan, M.; Cheng, H. On the CO₂ capture in water-free monoethanolamine solution: An ab initio molecular dynamics study. *J. Phys. Chem. B* **2013**, *117*, 5971–5977. [[CrossRef](#)] [[PubMed](#)]
21. Tian, Z.Q.; Dai, S.; Jiang, D.E. What can molecular simulation do for global warming? *WIREs Comput. Mol. Sci.* **2016**, *6*, 173–197. [[CrossRef](#)]
22. Jhon, Y.H.; Shim, J.G.; Kim, J.H.; Lee, J.H.; Jang, K.R.; Kim, J. Nucleophilicity and accessibility calculations of alkanolamines: Applications to carbon dioxide absorption reactions. *J. Phys. Chem. A* **2010**, *114*, 12907–12913. [[CrossRef](#)] [[PubMed](#)]

23. Turgman-Cohen, S.; Giannelis, E.P.; Escobedo, F.A. Transport properties of amine/carbon dioxide reactive mixtures and implications to carbon capture technologies. *ACS Appl. Mater. Interfaces* **2015**, *7*, 17603–17613. [[CrossRef](#)] [[PubMed](#)]
24. Farmahini, A.H.; Kvamme, B.; Kuznetsova, T. Molecular dynamics simulation studies of absorption in piperazine activated mdea solution. *Phys. Chem. Chem. Phys.* **2011**, *13*, 13070–13081. [[CrossRef](#)] [[PubMed](#)]
25. Yu, Y.S.; Lu, H.F.; Wang, G.X.; Zhang, Z.X.; Rudolph, V. Characterizing the transport properties of multiamine solutions for CO₂ capture by molecular dynamics simulation. *J. Chem. Eng. Data* **2013**, *58*, 1429–1439. [[CrossRef](#)]
26. Du, Q.; Freysz, E.; Shen, Y.R. Surface vibrational spectroscopic studies of hydrogen bonding and hydrophobicity. *Science* **1994**, *264*, 826–828. [[CrossRef](#)] [[PubMed](#)]
27. Benjamin, I. Chemical reactions and solvation at liquid interfaces: A microscopic perspective. *Chem. Rev.* **1996**, *96*, 1449–1475. [[CrossRef](#)] [[PubMed](#)]
28. Davidovits, P.; Kolb, C.E.; Williams, L.R.; Jayne, J.T.; Worsnop, D.R. Mass accommodation and chemical reactions at gas-liquid interfaces. *Chem. Rev.* **2006**, *106*, 1323–1354. [[CrossRef](#)] [[PubMed](#)]
29. Garrett, B.C.; Schenter, G.K.; Morita, A. Molecular simulations of the transport of molecules across the liquid/vapor interface of water. *Chem. Rev.* **2006**, *106*, 1355–1374. [[CrossRef](#)] [[PubMed](#)]
30. Lin, C.K.; Yang, L.; Hayashi, M.; Zhu, C.Y.; Fujimura, Y.; Shen, Y.R.; Lin, S.H. Theory and applications of sum-frequency generations. *J. Chin. Chem. Soc.* **2014**, *61*, 77–92. [[CrossRef](#)]
31. Nagata, Y.; Ohto, T.; Backus, E.H.G.; Bonn, M. Molecular modeling of water interfaces: From molecular spectroscopy to thermodynamics. *J. Phys. Chem. B* **2016**, *120*, 3785–3796. [[CrossRef](#)] [[PubMed](#)]
32. Perry, A.; Neipert, C.; Space, B.; Moore, P.B. Theoretical modeling of interface specific vibrational spectroscopy: Methods and applications to aqueous interfaces. *Chem. Rev.* **2006**, *106*, 1234–1258. [[CrossRef](#)] [[PubMed](#)]
33. Shen, Y.R.; Ostroverkhov, V. Sum-frequency vibrational spectroscopy on water interfaces: Polar orientation of water molecules at interfaces. *Chem. Rev.* **2006**, *106*, 1140–1154. [[CrossRef](#)] [[PubMed](#)]
34. Allinger, N.L.; Yuh, Y.H.; Lii, J.H. Molecular mechanics—The MM3 force-field for hydrocarbons.1. *J. Am. Chem. Soc.* **1989**, *111*, 8551–8566. [[CrossRef](#)]
35. Allinger, N.L.; Li, F.B.; Yan, L.Q. Molecular mechanics—The MM3 force-field for alkenes. *J. Comput. Chem.* **1990**, *11*, 848–867. [[CrossRef](#)]
36. Allinger, N.L.; Rahman, M.; Lii, J.H. A molecular mechanics force-field (MM3) for alcohols and ethers. *J. Am. Chem. Soc.* **1990**, *112*, 8293–8307. [[CrossRef](#)]
37. Lii, J.H.; Allinger, N.L. Molecular mechanics—The MM3 force-field for hydrocarbons. 2. Vibrational frequencies and thermodynamics. *J. Am. Chem. Soc.* **1989**, *111*, 8566–8575. [[CrossRef](#)]
38. Lii, J.H.; Allinger, N.L. Molecular mechanics—The MM3 force-field for hydrocarbons. 3. The vanderwaals potentials and crystal data for aliphatic and aromatic-hydrocarbons. *J. Am. Chem. Soc.* **1989**, *111*, 8576–8582. [[CrossRef](#)]
39. Lii, J.H.; Allinger, N.L. The MM3 force-field for amides, polypeptides and proteins. *J. Comput. Chem.* **1991**, *12*, 186–199. [[CrossRef](#)]
40. Wang, F.; Akin-Ojo, O.; Pinnick, E.; Song, Y. Approaching post-hartree-fock quality potential energy surfaces with simple pair-wise expressions: Parameterising point-charge-based force fields for liquid water using the adaptive force matching method. *Mol. Simul.* **2011**, *37*, 591–605. [[CrossRef](#)]
41. Akin-Ojo, O.; Song, Y.; Wang, F. Developing ab initio quality force fields from condensed phase quantum-mechanics/molecular-mechanics calculations through the adaptive force matching method. *J. Chem. Phys.* **2008**, *129*, 064108. [[CrossRef](#)] [[PubMed](#)]
42. Akin-Ojo, O.; Wang, F. Improving the point-charge description of hydrogen bonds by adaptive force matching. *J. Phys. Chem. B* **2009**, *113*, 1237–1240. [[CrossRef](#)] [[PubMed](#)]
43. Akin-Ojo, O.; Wang, F. The quest for the best nonpolarizable water model from the adaptive force matching method. *J. Comput. Chem.* **2011**, *32*, 453–462. [[CrossRef](#)] [[PubMed](#)]
44. Maillet, J.B.; Boutin, A.; Buttefey, S.; Calvo, F.; Fuchs, A.H. From molecular clusters to bulk matter: I. Structure and thermodynamics of small CO₂, N₂, and SF₆ clusters. *J. Chem. Phys.* **1998**, *109*, 329–337. [[CrossRef](#)]
45. Liu, H.B.; Jordan, K.D. Finite temperature properties of (CO₂)_n clusters. *J. Phys. Chem. A* **2003**, *107*, 5703–5709. [[CrossRef](#)]

46. Murthy, C.S.; O Shea, S.F.; McDonald, I.R. Electrostatic interactions in molecular-crystals-lattice-dynamics of solid nitrogen and carbon-dioxide. *Mol. Phys.* **1983**, *50*, 531–541. [[CrossRef](#)]
47. Monoethanolamine. Chemistry Webbook. Available online: <http://webbook.nist.gov> (accessed on 1 March 2015).
48. Ponder, J.W. Tinker, Version 7.1. Available online: <http://dasher.wustl.edu/tinker/> (accessed on 1 February 2015).
49. Becke, A.D. Density-functional exchange-energy approximation with correct asymptotic-behavior. *Phys. Rev. A* **1988**, *38*, 3098–3100. [[CrossRef](#)]
50. Lee, C.; Yang, W.; Parr, R.G. Development of the Colle-Salvetti correlation-energy formula into a functional of the electron density. *Phys. Rev. B* **1988**, *37*, 785–789. [[CrossRef](#)]
51. Grimme, S. Semiempirical gga-type density functional constructed with a long-range dispersion correction. *J. Comput. Chem.* **2006**, *27*, 1787–1799. [[CrossRef](#)] [[PubMed](#)]
52. Li, H.-C.; Chai, J.-D.; Tsai, M.-K. Assessment of dispersion-improved exchange-correlation functionals for the simulation of CO₂ binding by alcoholamines. *Int. J. Quantum. Chem.* **2014**, *114*, 805–812. [[CrossRef](#)]
53. Berendsen, H.J.C.; Postma, J.P.M.; Vangunsteren, W.F.; Dinola, A.; Haak, J.R. Molecular-dynamics with coupling to an external bath. *J. Chem. Phys.* **1984**, *81*, 3684–3690. [[CrossRef](#)]
54. Frisch, M.J.; Trucks, G.W.; Schlegel, H.B.; Scuseria, G.E.; Robb, M.A.; Cheeseman, J.R.; Scalmani, G.; Barone, V.; Mennucci, B.; Petersson, G.A.; et al. *Gaussian 09*; Gaussian, Inc.: Wallingford, CT, USA, 2009.

Sample Availability: Not available.



© 2016 by the authors; licensee MDPI, Basel, Switzerland. This article is an open access article distributed under the terms and conditions of the Creative Commons Attribution (CC-BY) license (<http://creativecommons.org/licenses/by/4.0/>).